Direct Numerical Simulation of Shock-wave/Isotropic Turbulence Interaction

Nathan E. Grube,* Ellen M. Taylor,† and M. Pino Martín‡
Princeton University, Princeton, NJ 08544 USA

We conduct direct numerical simulations (DNS) of shock/isotropic-turbulence interactions (SITI), in which the turbulence is highly compressible. We find, consistent with previous studies using weakly compressible turbulence, that turbulent kinetic energy and spanwise vorticity fluctuations become persistently amplified upon passage through a shock wave and that the spanwise Taylor microscale becomes persistently diminished. In addition, we find that the directional bias predictably introduced by the shock wave into the initially isotropic flow persists to some degree well downstream; and we also find that the shape of the shock wave becomes distorted by the passing turbulence to such a degree that sections of it may be found far upstream of its average position, causing statistical changes attributable to shock interaction to begin unexpectedly early.

I. Introduction

The interaction of turbulence with shock waves occurs in many external and internal fluid flows, including but not limited to flows over the surfaces of fast-moving vehicles and flows within the engines of such vehicles. Strong coupling between the two phenomena and strong nonlinearities in the interaction dynamics can lead to substantial changes in the structures of both the shock wave, which may impinge on surfaces at altered locations and with altered intensities, and the passing turbulence, which may cause physical mechanisms such as energy transfer to behave differently throughout the entire downstream region. The simplest shock/turbulence interaction configuration is that of homogeneous isotropic turbulence interacting with a steadily moving normal shock wave, but because of difficulties in forming such a configuration experimentally and adequately resolving it numerically, a much larger body of work exists for interactions of shock waves with turbulent boundary layers than for interactions with isotropic turbulence. While studies of shock/turbulent-boundary-layer interactions are of great importance from the standpoints of both physics and engineering, concurrent studies of shock/isotropic-turbulence interactions (SITI) can help to elucidate which physical processes are common to shock/turbulence interaction in general and which may be unique to interactions that include boundary layers.

Agui et al.[1] have produced the only experimental work on SITI involving turbulence that closely approaches isotropy, and numerical studies of low-Reynolds-number SITI in the form of direct numerical simulations (DNS) have been conducted by Hannappel and Friedrich,[2] Lee et al.,[3] Mahesh et al.,[4] and Jamme et al.[5] Together, these investigations confirm and elaborate on, among other findings, behaviors widely believed to be true of shock/turbulence interactions in general: certain turbulence properties, notably turbulent kinetic energy and vorticity fluctuations, are amplified upon passage through a shock wave and most turbulent length scales, such as the Taylor microscale, are diminished. In all of these studies, however, the upstream turbulence is incompressible or at most weakly compressible. In highly compressible isotropic turbulence, DNS by Passot and Pouquet,[6] Lee et al.,[7] and Samtaney et al.[8] have demonstrated the existence of small, transient shock waves known as shocklets, which due to locally strong compression are capable of affecting global flow dynamics out of proportion to their small volume fraction. It is therefore reasonable to suspect that the interaction of shock waves with highly compressible turbulence may exhibit characteristics that cannot be inferred from the results of interactions with weakly compressible turbulence.

*Graduate Student, Mechanical and Aerospace Engineering Department, Princeton University, AIAA Member.
†Research Associate, Mechanical and Aerospace Engineering Department, Princeton University.
‡Assistant Professor, Mechanical and Aerospace Engineering Department, Princeton University, AIAA Senior Member.

The purpose of this paper is to describe direct numerical simulations of highly compressible isotropic turbulence interacting with a normal shock wave, and to ascertain physically relevant flow characteristics and processes from the resulting data. Sections II and III present governing equations and the numerical methods employed to compute them. In Sections IV and V, we describe the computational configuration and flow conditions of the conducted SITI simulations. Section VI introduces our approaches to data analysis, Section VII presents the results, and conclusions are drawn in Section VIII.

II. Governing Equations

Shock/isotropic-turbulence interaction is governed by the three-dimensional compressible Navier-Stokes equations describing conservation of mass, momentum, and energy,

$$\frac{\partial \rho}{\partial t} + \frac{\partial}{\partial x_j}\left(\rho u_j\right) = 0 \tag{1}$$

$$\frac{\partial}{\partial t}\left(\rho u_i\right) + \frac{\partial}{\partial x_j}\left(\rho u_i u_j + p\,\delta_{ij} - \sigma_{ij}\right) = 0 \tag{2}$$

$$\frac{\partial}{\partial t}\left(\rho e\right) + \frac{\partial}{\partial x_j}\left[\left(\rho e + p\right) u_j - \sigma_{ij} u_i + q_j\right] = 0 \tag{3}$$

in which ρ is density, u_i is velocity in the i direction, p is pressure, and e is total energy per unit mass. The viscous stress tensor σ_{ij} is assumed to obey a linear stress-strain relationship,

$$\sigma_{ij} = \mu\left[\left(\frac{\partial u_i}{\partial x_j} + \frac{\partial u_j}{\partial x_i}\right) - \frac{2}{3}\frac{\partial u_k}{\partial x_k}\delta_{ij}\right] \tag{4}$$

in which viscosity μ depends only on temperature T through a power law[9] of the form

$$\mu = \mu_0\left(\frac{T}{T_0}\right)^n \tag{5}$$

in which μ_0 and T_0 are reference values that depend on the particular gas mixture. The heat flux q_i is computed through Fourier's law of heat conduction,

$$q_i = -k\frac{\partial T}{\partial x_i} \tag{6}$$

in which k is thermal conductivity.

The working fluid is air, which is treated as a perfect gas with gas constant $R = 287.1\,\mathrm{m}^2/\mathrm{s}^2K$ and constant specific heat capacity (at constant volume) $c_v = \frac{5}{2}R$. Therefore $P = \rho RT$, in which T is temperature; the speed of sound $a = \sqrt{\gamma RT}$, in which the heat capacity ratio $\gamma = \frac{7}{5}$; and

$$e = c_v T + \tfrac{1}{2}u_k u_k \tag{7}$$

The reference viscosity μ_0 is taken to be $1.789 \times 10^{-5}\,\mathrm{kg/m\,s}$ at a reference temperature $T_0 = 288.2\,\mathrm{K}$ in accordance with the standard atmosphere at sea level, and the exponent n in Eq. (5) is taken to be 0.76. The thermal conductivity k is assumed to be proportional to the viscosity μ with a constant of proportionality equal to $\left(c_v + \frac{9}{4}R\right)$.[10]

III. Numerical Methods

The detailed simulation of compressible turbulence requires numerical methods that simultaneously avoid excessive damping of spatial features over a large range of length scales and prevent spurious oscillations near shocks and shocklets through robust shock-capturing. Numerical schemes that were developed to satisfy these constraints include, among others, weighted essentially non-oscillatory (WENO) methods.[11,12] WENO schemes compute numerical fluxes using several different candidate stencils and form a final flux approximation by summing weighted contributions from each stencil. Thus they are nonlinear. Smoothness measurements cause stencils that span large flow field gradients to be assigned small relative weights so

that a nearly discontinuous shock would provide a weight of almost zero to any stencil containing it. In smooth regions, the relative values of the weights are designed to be optimal by some gauge such as maximum order of accuracy or maximum bandwidth-resolving efficiency. Martín et al.[13] demonstrate that a bandwidth-optimized symmetric WENO method[13–15] provides accurate results for direct numerical simulations of compressible isotropic turbulence and turbulent boundary layers. Therefore, in the current work, we employ a fourth-order-accurate version of this scheme to compute the convective terms of the governing equations.

To compute the viscous terms, we employ a simple fourth-order-accurate standard central difference scheme; and to integrate over time, we employ the third-order-accurate, low-storage Runge-Kutta method of Williamson[16] with a CFL number of 0.5.

IV. Computational Configuration

Many properties of the SITI configuration are determined by the properties of the separately established isotropic turbulence (IT) field that provides inflow turbulence. The physical domain for that inflow simulation is a three-dimensional elongated box with periodic boundary conditions. The box has two edges of length L and one of length $N_B L$ to encompass a sufficiently broad sampling of large-scale turbulence structures; an evenly-spaced Cartesian grid discretizes this domain into $N_B N^3$ points. Two non-dimensional parameters characterize the flow state: the Reynolds number based on the Taylor microscale

$$Re_\lambda = \frac{\langle\rho\rangle\, u'_{\text{rms}}\, \lambda}{\langle\mu\rangle} \tag{8}$$

in which u'_{rms} is the root-mean-squared fluctuating velocity (per component) and λ is the Taylor microscale; and the turbulent Mach number

$$M_t = \frac{q}{\langle a\rangle} \tag{9}$$

in which a is the speed of sound and q is the root-mean-squared fluctuating velocity magnitude. Note that Re_λ and M_t are not constant throughout an IT simulation because the global strength of the turbulent fluctuations steadily decays over time without external forcing, which we do not include. A randomized solenoidal approximation to isotropic turbulence serves as an initial flow field, and to transform it into realistic turbulence, we evolve this field through a transient period lasting on the order of τ_t, which is the initial state's reference time λ/u'_{rms}. Additional details about our IT simulations can be found in Taylor and Martín.[17] Although Mahesh et al.[4] artificially adjust the resulting IT field so that it conforms to Morkovin's hypothesis before entering the SITI domain, the present work follows Lee et al.[3] and omits this step.

To generate shock/isotropic-turbulence interaction, this elongated box of isotropic turbulence is convected through the inflow boundary of the SITI configuration at supersonic Mach number M, which constitutes a third governing parameter. Because this inflow is supersonic, the boundary conditions here are completely specified, and no further boundary treatment is necessary. Domain size and resolution in directions perpendicular to the mean flow are determined by the uniform edge length L and grid resolution N of the inflow IT field. Useful domain size parallel to the mean flow, which is chosen to be aligned with the x-axis, is designated L_x and need only be large enough to comfortably contain the corrugations and drift of the main shock wave that passing turbulence is known to cause. In the current work, $L_x = \frac{1}{2}L$. Within L_x there are N_x grid points in the streamwise direction, which are weakly clustered around the main shock wave, located at $\frac{1}{2}L_x$, according to the relationship

$$\tilde{x}(\tilde{\imath}) = \frac{\tilde{\imath} - \alpha\, f(\tilde{\imath})}{1-\alpha} \tag{10}$$

in which $\tilde{\imath} = i/\left(N_x - 1\right)$ and lies in the range $[0,1]$, $\tilde{x} = x/L_x$, and

$$f(\tilde{\imath}) = \frac{1}{2}\left(1 + \frac{\tanh\left[\beta\left(2\tilde{\imath}-1\right)\right]}{2\tanh\beta}\right) \tag{11}$$

After interacting with the main shock wave, the altered turbulence field approaches the outflow boundary at *sub*sonic speed. The single inward-traveling characteristic at the outflow gives one degree of freedom which we use to specify the pressure at the outflow boundary. As insurance against acoustic reflections, an L_s-wide sponge layer[4,18] designed to damp reflections is inserted between the end of the useful domain

and the outflow boundary. In the present work, $L_s \gtrsim \frac{1}{4}L_x$. The sponge layer damps the solution toward a prescribed uniform post-shock state with a pressure that matches the outflow pressure. The outflow pressure is chosen to minimize the drift of the shock, as described in the following section.

A sketch of the entire computational domain resulting from all of these arrangements is provided by Fig. 1. In Fig. 2, a representative instantaneous plot of density gradient and mass flux deviation contours illustrates the flow. While statistical quantities in isotropic turbulence are aggregated over three spatial dimensions at each point in time, in SITI they are aggregated over time and the two spanwise dimensions at each streamwise location. We define $\langle\eta\rangle$ as the time- and spanwise-aggregated average of a generic quantity η, η' as the associated root-mean-squared deviation (*not* the local deviation), and $\langle\langle\eta\rangle\rangle$ and η'' as the corresponding density-weighted (Favre) average and root-mean-squared deviation, respectively.

V. Flow Conditions

The inflow isotropic turbulence field is initialized with nominal Reynolds number $(Re_\lambda)_0 = 35$, nominal turbulent Mach number $(M_t)_0 = 1.3$, and sea-level atmospheric thermodynamic conditions and then evolved until the IT initialization transient has sufficiently subsided. After we introduce this instantaneous field into the SITI domain at mean convective Mach number M, resetting $t = 0$, we must allow its leading edge to fully propagate across the useful computational domain and allow transient processes in the subsonic post-shock region to subside before initiating the gathering of SITI statistics. The duration of the transient period, which ends at $t = t^*\tau_t$, is determined by visual inspection of a plot of mean shock location versus time (e.g., Fig. 3) Because the inflow IT field is periodic in all spatial directions, including the streamwise one, contributions to SITI statistics cease to contain independent information at $t = (t^* + t^\circ)\,\tau_t$, in which

$$t^\circ = \frac{N_B L}{\tau_t U_E} \tag{12}$$

and therefore the gathering of statistics is halted at this time. Table 1 lists the physical and computational parameters for the SITI simulation that we conduct. The inflow turbulence is evolved until the initially solenoidal field has attained a physically realistic state. We consider the turbulence to have reached a realistic state when the skewness of the velocity derivatives has ceased to change rapidly, which in this case occurs by $t = 1.5\tau_t$. The isotropic turbulence is convected toward the shock-wave at Mach 5.

If the mean location of the shock moves up- or downstream during the collection of statistical data, the resulting profiles will appear smeared out, obscuring some of the finer details of the interaction. Upstream turbulent fluctuations primarily determine the shock corrugation and overall motion, and, because the inflow data is periodic in time, the shock motion is also nearly periodic in time. However, the mean shock motion usually exhibits an up- or downstream bias (or "shock drift"). This shock drift can be controlled using the specification of a back pressure at the domain outflow boundary. Multiple simulations for a given flow condition must be run in order to determine the exit pressure that leads to a shock that is stationary in the mean. The (turbulent) simulation is first run using the back pressure that is predicted to give a stationary shock in *laminar* flow. Then, the resulting mean shock drift velocity is measured after initial transients have subsided. The Rankine-Hugoniot jump condition is analytically differentiated to estimate the sensitivity of the shock drift speed to the back pressure, and a second simulation is run using the back pressure that is predicted to give a stationary shock in the presence of turbulence. The shock drift is a function of grid resolution. The simulation on the $160^2 \times 80$ point grid exhibited negligible drift during the first simulation; the mean shock drift over the data collection period was an order of magnitude less than the random mean shock motion due to turbulent fluctuations (and also an order of magnitude smaller than the root-mean-square deviation from the instantaneous mean location caused by corrugations). However, the simulation on $192^2 \times 96$ grid points required a second run in order to achieve a similarly stationary shock (see Fig. 3). A variety of root-finding algorithms can be used to select back pressures for successive simulations to give smaller and smaller shock drifts. A third run on $192^2 \times 96$ grid points using linear extrapolation of the drifts from the first two runs gave still better results. Results for a finer $240^2 \times 120$ point grid indicate that the shock drift worsens with grid refinement, and, for this grid, three runs are needed in order to achieve a shock drift an order of magnitude smaller than the random shock motion. Studies on coarser grids (not discussed here) suggest that the shock drift can be reduced to arbitrarily small values as long as the same initial data and stopping time are used for each run.

Figure 4 displays streamwise profiles of root-mean-squared deviations of temperature and kinetic energy

and profiles of spanwise Taylor microscale as computed on a grid of $160^2 \times 80$ points, on a grid 20% finer ($192^2 \times 96$), and on a grid 20% finer still ($240^2 \times 120$). There are no evident differences in temperature or kinetic energy fluctuations between the grids. (A shift in the streamwise direction has no physical significance.) Although there are differences in Taylor microscale, especially where the streamwise profile reaches its minimum, these differences are not large and are in no way qualitative, and, importantly, their magnitudes do not grow as the flow travels downstream. Therefore, we deem the SITI simulations to be nearly grid-converged. Simulations with still finer grids are underway. Unless otherwise noted, all plots show data from the $192^2 \times 96$ point grid. Additionally, in Fig. 5, we show these same flow properties as computed by considering half as much inflow data. There are no significant differences in temperature fluctuations, kinetic energy fluctuations, or Taylor microscale. Thus, in general, we deem the statistics of SITI simulations conducted according to Section IV to be sufficiently time-converged. Unless otherwise noted, all results presented here are based on inflow data with $N_B = 25$, which leads to $t^\circ \approx 60$.

VI. Approaches to Data Analysis

Before presenting our results in the next section, we establish groundwork regarding our approaches to analyzing the three-dimensional unsteady flow data of shock/isotropic-turbulence interaction. These approaches consist of plots of streamwise profiles of time- and spanwise-averaged flow properties, including thermodynamic and vorticity fluctuations, Taylor microscale, velocity-temperature correlation, and budgets of vorticity and Reynolds stresses; and plots of time-averaged three-dimensional kinetic energy spectra at key streamwise locations.

The signed streamwise-velocity/temperature correlation R_{uT} is useful for gauging the disequilibrium of turbulent fluid flow. We compute it using density-weighted statistics such that

$$R_{uT} = \frac{\left\langle\!\left\langle \left(u_x - \langle\!\langle u_x \rangle\!\rangle\right)\left(T - \langle\!\langle T \rangle\!\rangle\right) \right\rangle\!\right\rangle}{u_x'' T''} \tag{13}$$

Budgets of vorticity and Reynolds stresses serve to segregate total changes in these two properties into contributions from different physical processes. Conservation of vorticity is characterized by the following adaptation of Eq. (2):

$$\frac{D\vec{\omega}}{Dt} = \left(\vec{\omega}\cdot\vec{\nabla}\right)\vec{u} - \vec{\omega}\left(\vec{\nabla}\cdot\vec{u}\right) + \frac{1}{\rho^2}\vec{\nabla}\rho\times\vec{\nabla}p + \vec{\nabla}\times\frac{1}{\rho}\left(\vec{\nabla}\cdot\vec{\bar{\sigma}}\right) \tag{14}$$

in which $\vec{\omega}$ is the vorticity vector and $\frac{D}{Dt}$ is the material derivative operator. From left to right, the quantities on the right-hand side of this equation describe stretching and tilting due to velocity gradients, stretching due to flow compressibility, changes due to the misalignment of density and pressure surfaces, and changes due to diffusion. We refer to them as the stretching, compressible, baroclinic, and diffusion terms, respectively. Conservation of Reynolds stresses is characterized by the following alternative adaptation of Eq. (2), which omits certain negligible terms that approach zero as the flow approaches incompressibility:

$$\frac{\langle\!\langle D \rangle\!\rangle}{\langle\!\langle D \rangle\!\rangle t} R_{ij} = -\frac{\partial}{\partial x_k} T_{ijk} + \mathcal{P}_{ij} + \Pi_{ij} + \phi_{ij} - \varepsilon_{ij} \tag{15}$$

in which

$$\frac{\langle\!\langle D \rangle\!\rangle}{\langle\!\langle D \rangle\!\rangle t} = \frac{\partial}{\partial t} + \langle\!\langle u_k \rangle\!\rangle \frac{\partial}{\partial x_k} \tag{16}$$

$$R_{ij} = \left\langle \rho u_i'' u_j'' \right\rangle \tag{17}$$

$$T_{ijk} = \left\langle \rho u_i'' u_j'' u_k'' \right\rangle \tag{18}$$

$$\mathcal{P}_{ij} = -R_{jk}\frac{\partial \langle\!\langle u_i \rangle\!\rangle}{\partial x_k} - R_{ik}\frac{\partial \langle\!\langle u_j \rangle\!\rangle}{\partial x_k} - R_{ij}\frac{\partial \langle\!\langle u_k \rangle\!\rangle}{\partial x_k} \tag{19}$$

$$\Pi_{ij} = -\left\langle u_i''\frac{\partial p'}{\partial x_j} + u_j''\frac{\partial p'}{\partial x_i} \right\rangle \tag{20}$$

$$\phi_{ij} = \frac{\partial}{\partial x_k}\left\langle u_i''\sigma_{jk}' + u_j''\sigma_{ik}' \right\rangle \tag{21}$$

$$\varepsilon_{ij} = \left\langle \sigma'_{jk} \frac{\partial u''_i}{\partial x_k} + \sigma'_{ik} \frac{\partial u''_j}{\partial x_k} \right\rangle \tag{22}$$

and, in this instance only, the prime and double-prime superscripts indicate instantaneous rather than root-mean-squared deviations. From left to right, the quantities on the right-hand side of Eq. (15) are known as the turbulent convection, production, pressure, viscous diffusion, and viscous dissipation terms.

As stated previously, streamwise profiles of flow properties are created by statistically aggregating local instantaneous values over time and the two spanwise spatial dimensions at each streamwise location. Although we adjust the exit pressure to mitigate the shock drift, the passing turbulent fluctuations still lead to substantial random streamwise motion and corrugation of the main shock wave. Therefore, the shock's broad effects on that turbulence cannot be localized to a single streamwise location but are rather spread over a range. Let us define $\langle x_s \rangle_{\min}$ as the minimum instantaneous spanwise-averaged position, $\langle x_s \rangle_{\max}$ as the maximum instantaneous average, and x'_s as the time-averaged root-mean-squared deviation from instantaneous average. In all plots of streamwise profiles, a shaded region bounded by dashed lines will denote the region between $\langle x_s \rangle_{\min}$ and $\langle x_s \rangle_{\max}$, and dotted lines upstream and downstream of this region will denote, respectively, $\langle x_s \rangle_{\min} - x'_s$ and $\langle x_s \rangle_{\max} + x'_s$. We consider the entire area between the latter bounds to constitute the interaction region.

Determining the instantaneous local streamwise positions of the main shock wave, which are necessary for computing the statistical quantities above, is in general not trivial to accomplish both accurately and efficiently. We begin by identifying, for each point in time separately, the m strongest density and pressure gradients along a streamwise line through each spanwise grid location under the assumption that such gradients must traverse either the main shock wave or especially strong shocklets. These locations are then ranked by how closely the strengths of the shock wave sections that coincide with them conform to the prescribed average strength of the main shock wave. We use the single most attractive candidate position (according to this ranking) at each spanwise location to calculate a preliminary instantaneous average streamwise position and root-mean-squared deviation; we then temporarily discard any points that lie more than twice this root-mean-squared deviation away from this average; and we use the remaining points to calculate a new conditionally spanwise-averaged main shock position. For the outlier points that were temporarily discarded, we substitute whichever one of the m candidates at those spanwise locations that minimizes deviation from the conditional average under the assumption that the main shock wave should be relatively continuous. In all conducted SITI simulations, we find that setting $m = 2$ provides sufficient accuracy.

Finally, at key streamwise locations, we compute the three-dimensional turbulent kinetic energy spectrum

$$E_T(k) = \tfrac{1}{2} \hat{\vec{u}}(k) \cdot \hat{\vec{u}}(k) \tag{23}$$

in which carats indicate Fourier transforms and k is wavenumber magnitude, using the two spanwise directions and the transformed time history of the flow across the spanwise plane. This energy spectrum can be decomposed into contributions $E_I(k)$ and $E_C(k)$ from, respectively, incompressible (divergence-free) components of velocity $\hat{\vec{u}}_I$ and compressible (curl-free) components of velocity $\hat{\vec{u}}_C$, in which

$$\hat{\vec{u}}_C = \tfrac{\vec{k} \cdot \hat{\vec{u}}}{k^2} \vec{k} \tag{24}$$

$$\hat{\vec{u}}_I = \hat{\vec{u}} - \hat{\vec{u}}_C \tag{25}$$

A measure of overall flow compressibility is then provided by the relative compressible energy ratio

$$\chi = \frac{\int E_C(k)\ dk}{\int E_T(k)\ dk} \tag{26}$$

VII. Results

The interaction of the shock with the passing turbulence causes a marked but temporary increase in the fluctuating thermodynamic properties. In Fig. 6, we plot streamwise profiles of root-mean-squared deviations of density, pressure, and temperature for these cases. All properties decay from the inlet as the turbulence naturally dissipates, then temporarily spike across the interaction region, and then resume nearly original

decay trajectories. It is interesting to note that the greatest thermodynamic fluctuations occur toward the upstream side of the interaction region, with the peak in temperature fluctuations occurring significantly upstream of the interaction region as defined in section VI. It seems that relatively rare events which cause the shock to move farthest upstream also cause the largest temperature fluctuations.

The interaction of the shock wave with the turbulence also has a significant effect on the fluctuating vorticity. Figure 7 shows streamwise profiles of root-mean-squared deviations of stream- and spanwise vorticity. The interaction leads to amplified levels of both streamwise and spanwise vorticity fluctuations, which a much larger amplification of spanwise vorticity. As the turbulence convects away from the interaction region, the vorticity still possesses increased intensity, but begins to return toward a more isotropic state. The vorticity amplification can be better understood by analyzing the vorticity conservation budget (14) term-by-term. Because of the symmetry of the problem, the mean vorticity must be statistically zero everywhere. However, the interaction amplifies the fluctuating vorticity. In order to investigate the effect of each budget term on the vorticity fluctuations, we average the terms in the spanwise direction after selecting a sign conditioned by the sign of the local instantaneous vorticity fluctuation. If a budget term acts to drive the fluctuation toward zero, it will decrease the RMS vorticity fluctuation and hence is taken to have a negative sign. Budget terms driving fluctuations away from zero are taken to have positive contributions. Figure 8 plots the resulting budgets. The compressible term has the greatest effect, causing an increase in both components of fluctuating vorticty. The increase in the streamwise component is approximately one third as great and is partially offset by a negative contribution from the stretching term. The overall effect is a much greater increase in the levels of spanwise vorticity than streamwise.

The largest scales of the turbulence are determined by the properties of the isotropic turbulence at the inlet and are not changed in the spanwise directions by the interaction, so the large scales of the flow may be expected to remain nearly constant. However, the interaction energizes the turbulence and therefore causes reductions in the Taylor microscales and Kolmogorov scale. Figure 9 shows streamwise profiles of stream- and spanwise Taylor microscales and the Kolmogorov scale. Although the streamwise Taylor microscale recovers to approximately its pre-shock value, the spanwise microscale and the Kolmogorov scale remain diminished. Also shown is a profile of R_{uT}, the correlation coefficient between (Favre) fluctuations in temperature and streamwise velocity. This correlation coefficient gives a measure of the disequilibrium of the flow.

Streamwise profiles of root-mean-squared deviations of streamwise mass flux and kinetic energy are plotted in Figure 10 along with the compressible energy ratio χ. The interaction amplifies fluctuations in both mass flux and kinetic energy as well as increasing the fraction of turbulent kinetic energy that is compressible modes.

Figure 11 shows the individual contributions of the terms in the Reynolds Stress budget (15). For the streamwise-streamwise stress, the diffusion term is negligible and the dissipation term is small relative to the other three terms; and across the interaction region, there is destruction flanked by lesser creation on the part of the convective term, creation on the part of the production term, creation followed by destruction on the part of the pressure term, and destruction on the part of the dissipation term. For spanwise-spanwise stress, the diffusion term is again negligible and the convection and dissipation terms are modest relative to the other two terms; and across the interaction region, creation and destruction patterns are similar to those of the streamwise-streamwise stress budget, except that the leading creation on the part of the pressure term is more pronounced than the trailing destruction. Note that non-negligible dissipation persists downstream, where it is unbalanced by the other terms. Note that all budget terms are approximately an order of magnitude smaller for the spanwise-spanwise stress than for the streamwise-streamwise stress. The streamwise-spanwise stress should be statistically zero, and indeed the budget terms are approximately another order of magnitude smaller.

Figure 12 plots the three-dimensional turbulent kinetic energy spectra at the domain inlet and at the boundaries of the interaction region. The spectra considering only energy in compressible modes are also plotted. Aside from a slight filling-out of the lowest wavenumber solenoidal modes, there is little qualitative change in the spectrum as the turbulence convects downstream toward the interaction region. After the turbulence has crossed the shock, however, there is a marked increase in the energy of the higher wavenumber modes. Most of the increase in energy is due to amplification of the compressible modes.

VIII. Conclusion

We have presented a direct numerical simulation of highly-compressible isotropic turbulence interacting with a strong shock wave. The computational configuration is described along with an outflow boundary condition designed to minimize shock drift. Statistical convergence of the DNS data is shown. The data are believed to be nearly grid-converged, but simulations on finer grids are underway to verify this. The flow field is described through the interaction. An assessment of the interaction dynamics is currently ongoing by considering and comparing the current case to other limiting cases.

Acknowledgments

This work is sponsored in part by AFOSR Grant FA9550-06-1-0323, NASA CUIP Award NCC3-989, and NASA Grant number NNX08AD04A. Computational resources were provided by the CRoCCo Laboratory at Princeton University.

References

[1]Agui, J. H., Briassulis, G., and Andreopoulos, Y., "Studies of interactions of a propagating shock wave with decaying grid turbulence: velocity and vorticity fields," *Journal of Fluid Mechanics*, Vol. 524, 2005, pp. 143–95.

[2]Hannappel, R. and Friedrich, R., "Direct numerical simulation of a Mach 2 shock interacting with isotropic turbulence," *Applied Scientific Research*, Vol. 54, No. 3, 1995, pp. 205–21.

[3]Lee, S., Lele, S. K., and Moin, P., "Interaction of isotropic turbulence with shock waves: Effect of shock strength," *Journal of Fluid Mechanics*, Vol. 340, 1997, pp. 225–47.

[4]Mahesh, K., Lele, S. K., and Moin, P., "The influence of entropy fluctuations on the interaction of turbulence with a shock wave," *Journal of Fluid Mechanics*, Vol. 334, 1997, pp. 353–79.

[5]Jamme, S., Cazalbou, J.-B., Torres, F., and Chassaing, P., "Direct numerical simulation of the interaction between a shock wave and various types of isotropic turbulence," *Flow, Turbulence and Combustion*, Vol. 68, No. 3, 2002, pp. 227–68.

[6]Passot, T. and Pouquet, A., "Numerical simulation of compressible homogeneous flows in the turbulent regime," *Journal of Fluid Mechanics*, Vol. 181, 1987, pp. 441–66.

[7]Lee, S., Lele, S. K., and Moin, P., "Eddy shocklets in decaying compressible turbulence," *Physics of Fluids A*, Vol. 3, No. 4, 1991, pp. 657–64.

[8]Samtaney, R., Pullin, D. I., and Kosović, B., "Direct numerical simulation of decaying compressible turbulence and shocklet statistics," *Physics of Fluids*, Vol. 13, No. 5, 2001, pp. 1415–30.

[9]White, F. M., *Viscous Fluid Flow*, McGraw-Hill, 2nd ed., 1991.

[10]Vincenti, W. G. and Kruger, C. H., *Introduction to Physical Gas Dynamics*, John Wiley and Sons, 1965.

[11]Liu, X.-D., Osher, S., and Chan, T., "Weighted Essentially Non-Oscillatory Schemes," *Journal of Computational Physics*, Vol. 115, No. 1, 1994, pp. 200–12.

[12]Jiang, G.-S. and Shu, C.-W., "Efficient implementation of weighted ENO schemes," *Journal of Computational Physics*, Vol. 126, No. 1, 1996, pp. 202–28.

[13]Martín, M. P., Taylor, E. M., Wu, M., and Weirs, V. G., "A bandwidth-optimized WENO scheme for the effective direct numerical simulation of compressible turbulence," *Journal of Computational Physics*, Vol. 220, No. 1, 2006, pp. 270–89.

[14]Weirs, V. G. and Candler, G. V., "Optimization of weighted ENO schemes for DNS of compressible turbulence," Paper 1997–1940, American Institute of Aeronautics and Astronautics, 1997.

[15]Weirs, V. G., *A Numerical Method for the Direct Simulation of Compressible Turbulence*, Ph.D. thesis, University of Minnesota, December 1998.

[16]Williamson, J. H., "Low-storage Runge-Kutta schemes," *Journal of Computational Physics*, Vol. 35, No. 1, 1980, pp. 48–56.

[17]Taylor, E. M. and Martín, M. P., "Stencil adaptation properties of a WENO scheme in direct numerical simulations of compressible turbulence," *Journal of Scientific Computing*, Vol. 30, No. 3, 2007, pp. 533–54.

[18]Israeli, M. and Orszag, S. A., "Approximation of radiation boundary conditions," *Journal of Computational Physics*, Vol. 41, No. 1, 1981, pp. 115–35.

Case	coarse	fine	finer
M	5.0	–	–
$(Re_\lambda)_0$	35	–	–
$(M_t)_0$	1.3	–	–
$(Re_\lambda)_E$	19.8	19.6	19.6
$(M_t)_E$	0.893	0.894	0.896
N^2	160^2	192^2	240^2
N_x+N_s	80+20	96+24	120+30
t^*	37.0	–	–
t°	97.5	–	–
α	$\frac{1}{8}$	–	–
β	2	–	–

Table 1. Physical and computational parameters for conducted simulations of shock/isotropic-turbulence interaction.

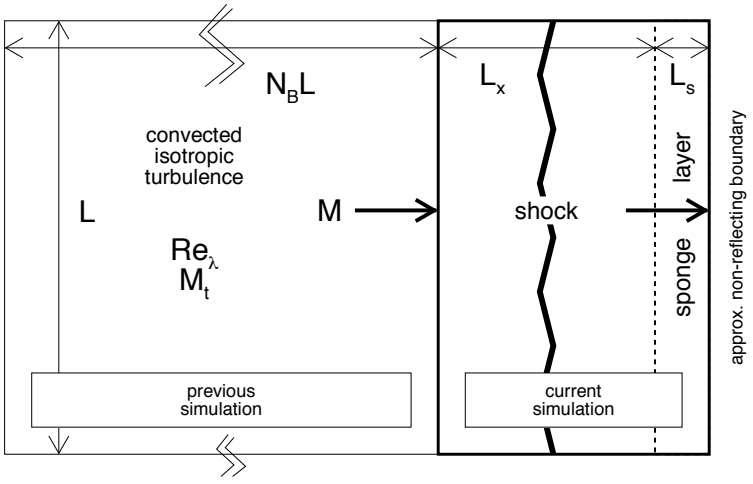

Figure 1. Computational domain sketch for shock/isotropic-turbulence interaction.

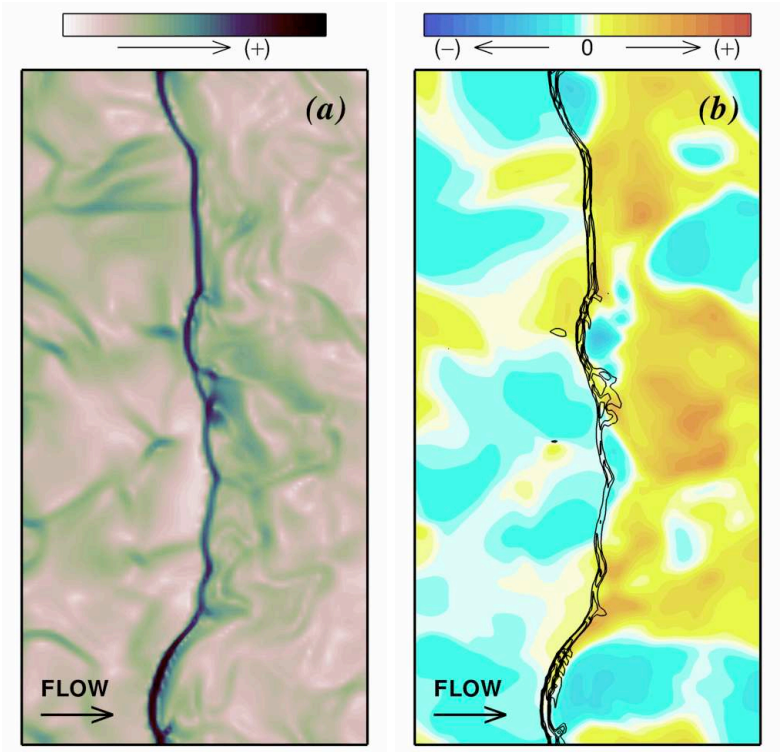

Figure 2. Instantaneous cross sections of *(a)* density gradient magnitude $|\nabla\rho| \,/\, \langle\rho\rangle$ and *(b)* mass flux deviation $(\rho u_x - \langle\rho u_x\rangle) \,/\, \langle\rho u_x\rangle$ with density gradient magnitude overlayed for reference (enhanced online).

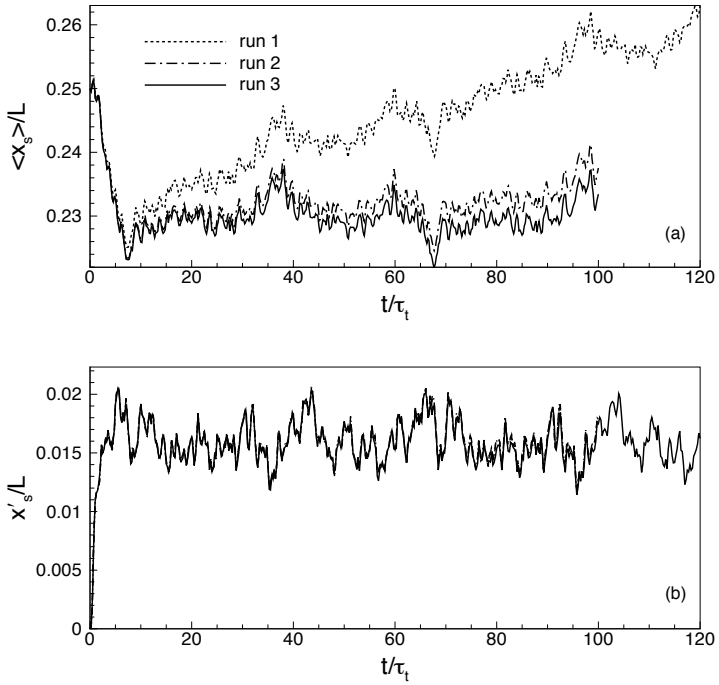

Figure 3. Shock drift and corrugation as measured by time histories of *(a)* mean (spanwise-averaged) shock location, and *(b)* root-mean-squared deviations of local shock location from mean shock location. Run 1 prescribed an exit pressure equal to that of the laminar post-shock state, Run 2 prescribed an exit pressure corrected using the analytically differentiated jump condition, and Run 3 used linear extrapolation of the results from the first two runs to prescribe an exit pressure which further reduces the shock drift.

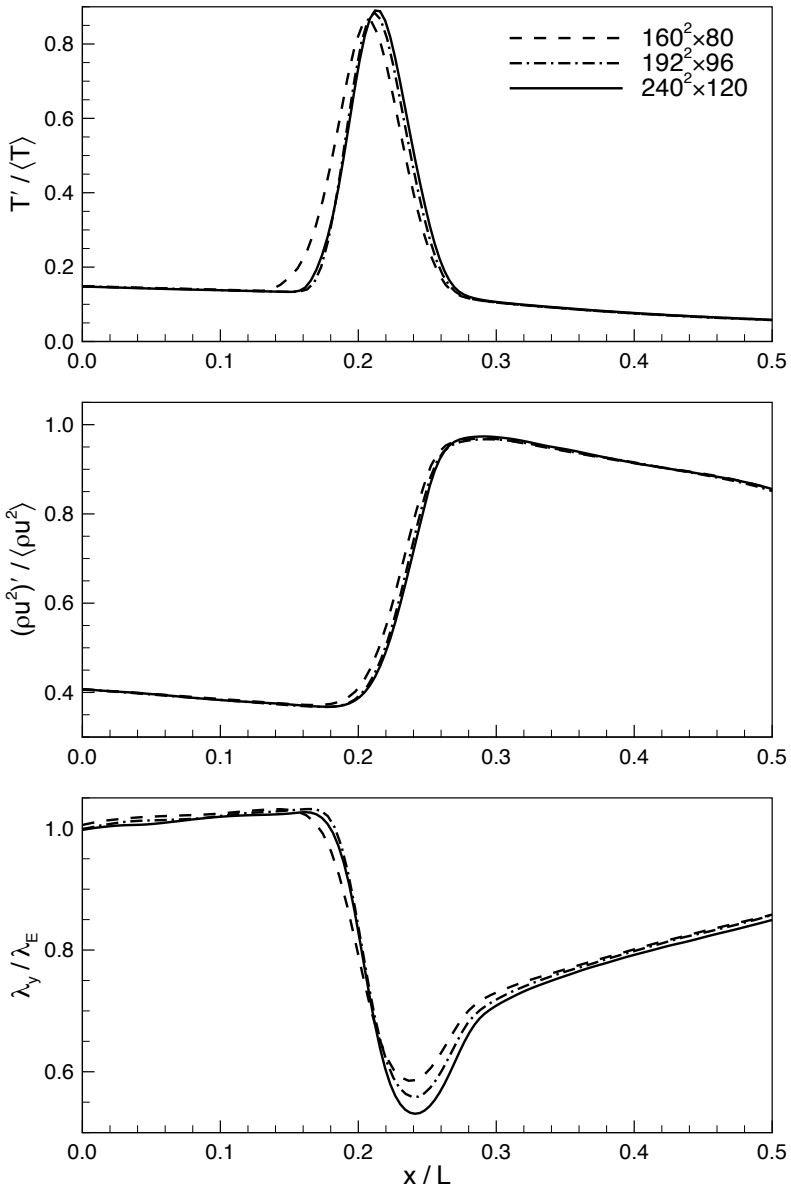

Figure 4. Streamwise profiles of *(a)* root-mean-squared deviations of temperature, *(b)* root-mean-squared deviations of kinetic energy, and *(c)* spanwise Taylor microscale, as computed on grids of $160 \times 160 \times 80$, $192 \times 192 \times 96$, and $240 \times 240 \times 120$ points.

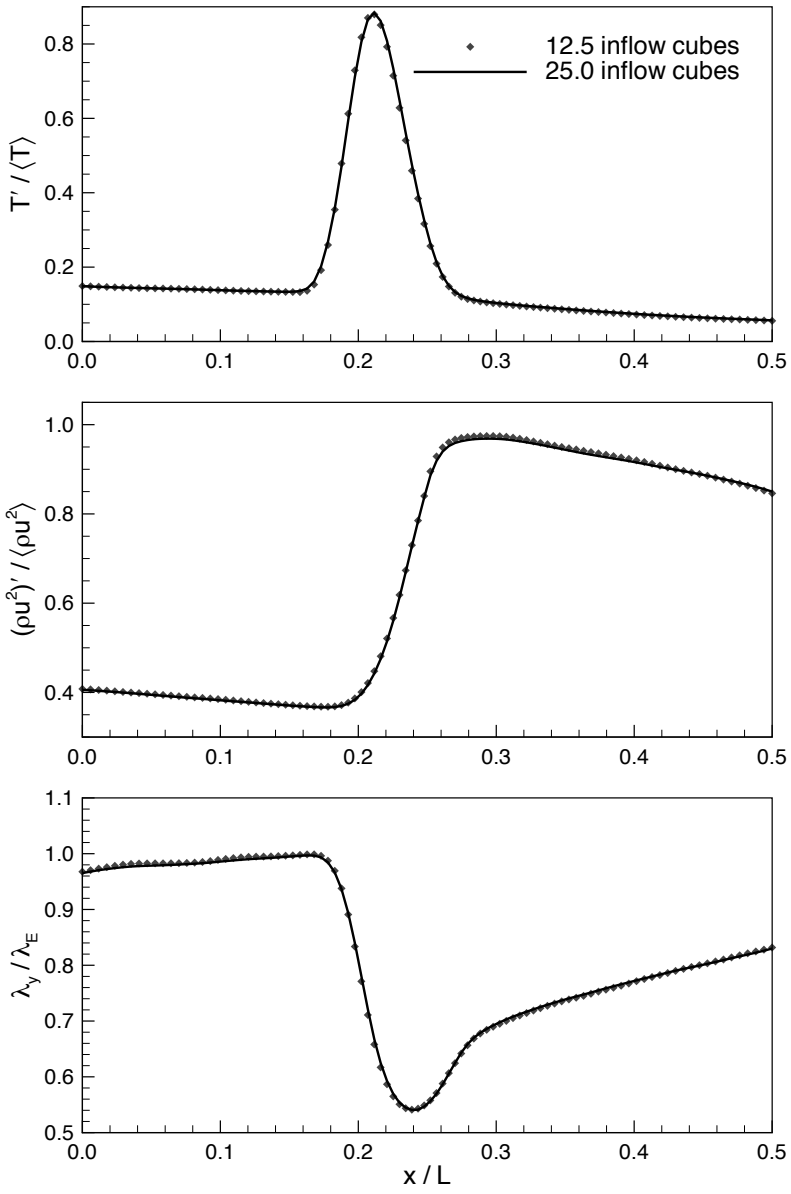

Figure 5. Streamwise profiles of *(a)* root-mean-squared deviations of temperature, *(b)* root-mean-squared deviations of kinetic energy, and *(c)* spanwise Taylor microscale, as computed by gathering statistics for $t^\circ \approx 30$ and $t^\circ \approx 60$, which correspond to $N_B = 12.5$ and $N_B = 25$.

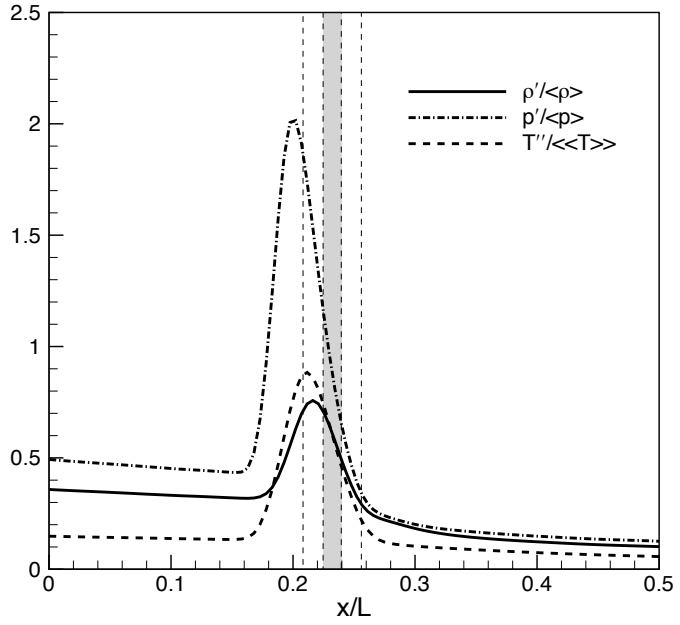

Figure 6. Streamwise profiles of root-mean-squared deviations of density, pressure, and temperature.

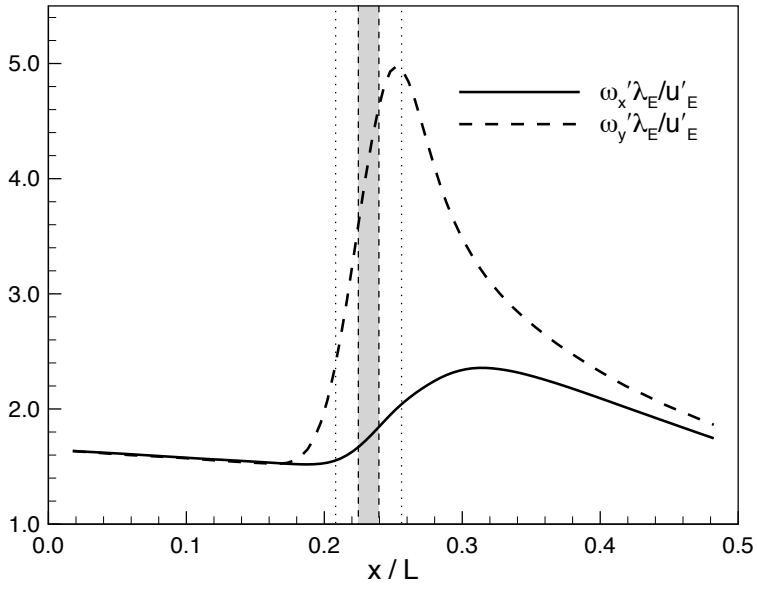

Figure 7. Streamwise profiles of root-mean-squared deviations of stream- and spanwise vorticity.

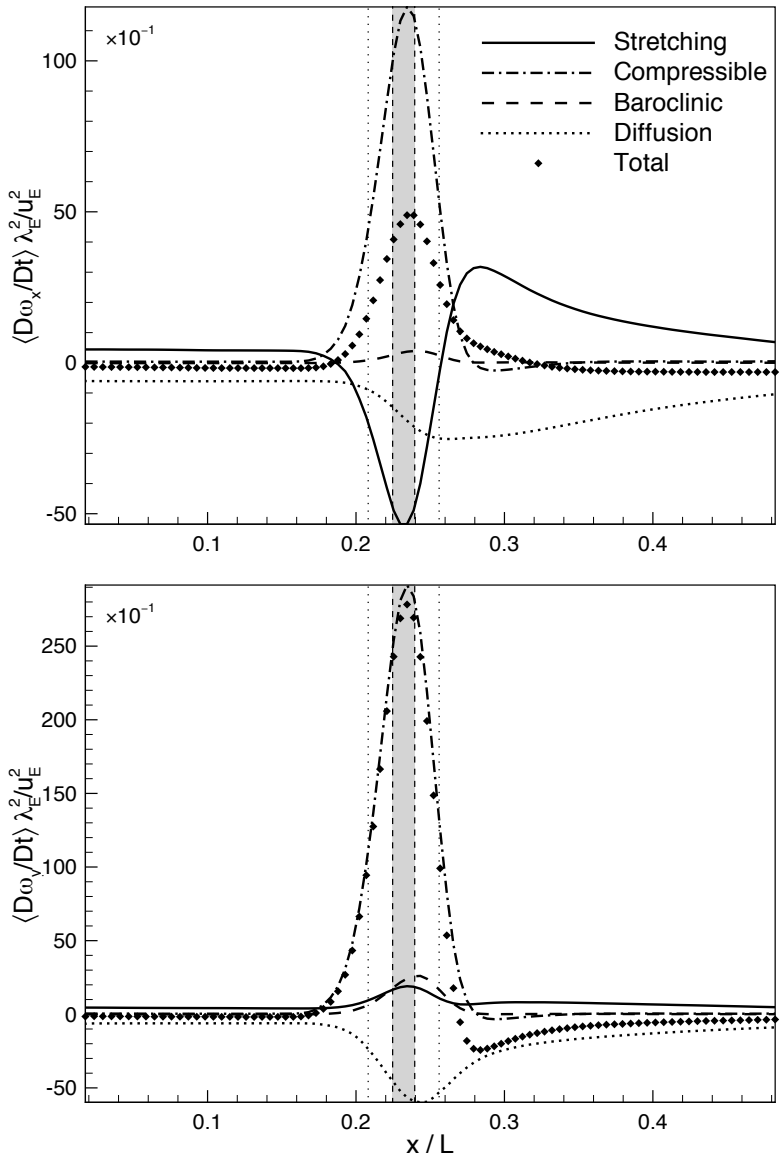

Figure 8. Streamwise profiles (averaged using sign conditioned on sign of vorticity) of contributions to total changes in *(a)* streamwise and *(b)* spanwise vorticity components.

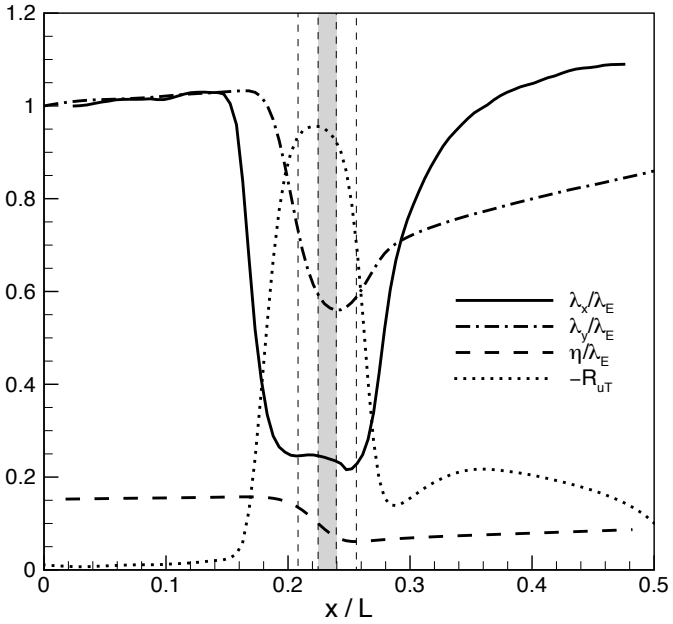

Figure 9. Streamwise profiles of turbulent lengthscales: stream- and spanwise Taylor microscales and the Kolmogorov scale. Also shown is the negative streamwise velocity-temperature correlation coefficient.

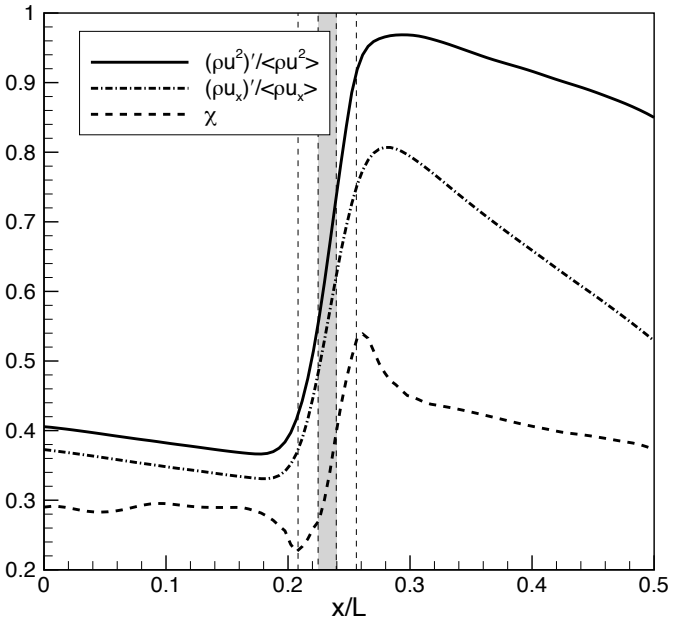

Figure 10. Streamwise profiles of root-mean-squared deviations of kinetic energy and streamwise mass flux along with compressible energy ratio for *(a)* Case C2 ($M = 2$) versus *(b)* Case C3 ($M = 5$).

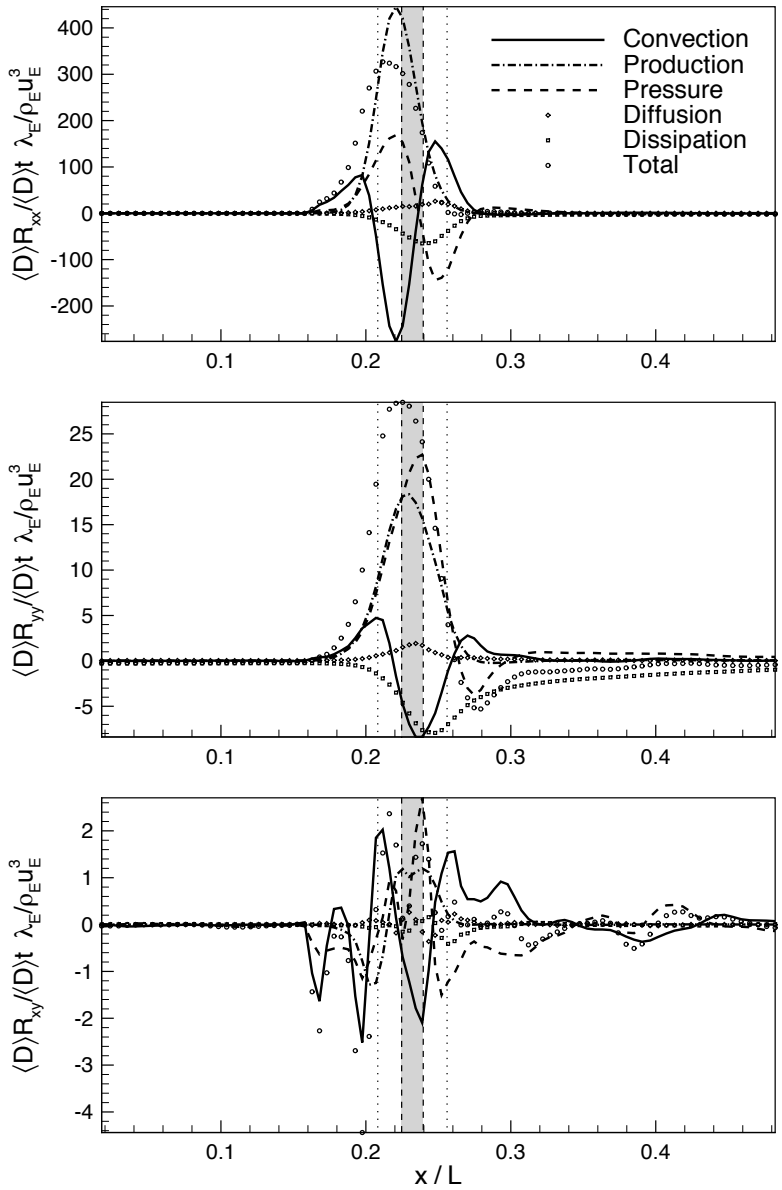

Figure 11. Streamwise profiles of contributions to total changes in *(a)* streamwise-streamwise, *(b)* spanwise-spanwise, and *(c)* streamwise-spanwise Reynolds stresses.

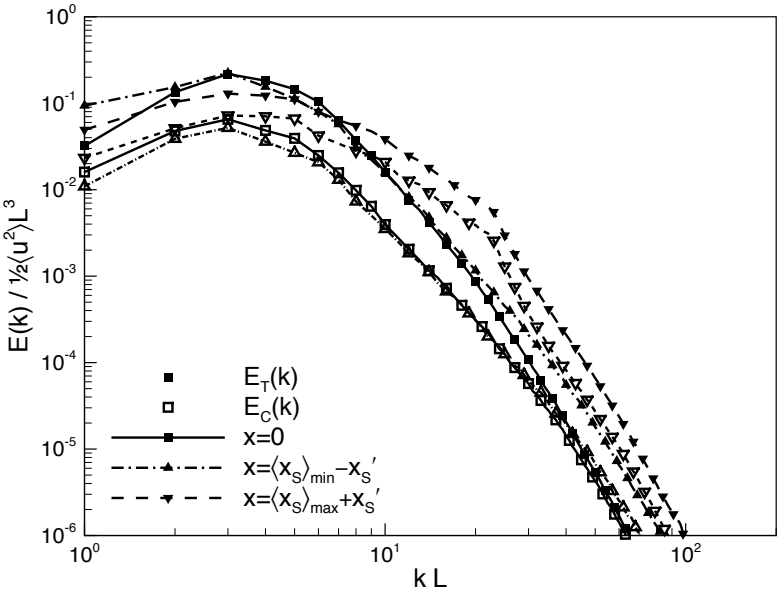

Figure 12. Three dimensional turbulent kinetic energy spectra at the upstream and down stream edges of the interaction region given by $x =< x_s >_{\min} -x_s'$ and $x =< x_s >_{\max} +x_s'$